Stretchable conductors by kirigami patterning of aramid-silver nanocomposites with zero conductance gradient

Jing Lyu,[1,2,3] Mark D. Hammig,[4] Lehao Liu,[1,2,3] Lizhi Xu,[1,2] Hang Chi,[5] Ctirad Uher,[5] Tiehu Li,[3] and Nicholas A. Kotov[1,2,6,7,8,a]

[1]Department of Chemical Engineering, University of Michigan, Ann Arbor, Michigan 48109, USA
[2]Biointerfaces Institute, University of Michigan, Ann Arbor, Michigan 48109, USA
[3]School of Materials Science and Engineering, Northwestern Polytechnical University, Xi'an 710072, People's Republic of China
[4]Department of Nuclear Engineering and Radiological Sciences, University of Michigan, Ann Arbor, Michigan 48109, USA
[5]Department of Physics, University of Michigan, Ann Arbor, Michigan 48109, USA
[6]Department of Materials Science and Engineering, University of Michigan, Ann Arbor, Michigan 48109, USA
[7]Department of Biomedical Engineering, University of Michigan, Ann Arbor, Michigan 48109, USA
[8]Michigan Center for Integrative Research in Critical Care, 2800 Plymouth Road, Ann Arbor, Michigan 48109, USA

Materials that are both stretchable and electrically conductive enable a broad spectrum of applications in sensing, actuating, electronics, optics and energy storage. The materials engineering concept of stretchable conductors is primarily based on combining nanowires, nanoribbons, nanoparticles, or nanocarbons with rubbery polymers to obtain composites with different abilities to transport charge and alter their nanoscale organization under strain. Although some of these composites reveal remarkably interesting multiscale reconfigurability and self-assembly phenomena, decreasing conductance with increased strain has restricted their widespread implementation. In a broader physical sense, the dependence of conductance on stress is undesirable because it requires a correlated change of electrical inputs. In this paper, we describe highly conductive and deformable sheets with a conductivity as high as $230\,000\,S\,cm^{-1}$, composed of silver nanoparticles, infiltrated within a porous aramid nanofiber (ANF) matrix. By forming a kirigami pattern, consisting of a regularized network of notches cut within the films, their ultimate tensile strain is improved from $\sim$2% to beyond 100%. The use of ANFs derived from well-known ultrastrong Kevlar™ fibers imparts high mechanical performance to the base composite. Importantly, the conductance of the films remains constant, even under large deformation resulting in a material with a zero conductance gradient. Unlike other nanocomposites for which strain and conductance are strongly coupled, the kirigami nanocomposite provides a pathway to demanding applications for flexible and stretchable electronics with power/voltage being unaffected by the deformation mode and temperature. *Published by AIP Publishing.* https://doi.org/10.1063/1.5001094

New types of electrical conductors are needed for electronic devices with form-factor flexibility.[1,2] Recently, various types of stretchable conductors have been designed and fabricated, using two complementary strategies.[3–5] The first one is based on stretchable materials, while the other depends on stretchable structural layouts.[6] Inorganic and organic conductive materials in micro- or nano-structured forms, intimately integrated with elastomeric polymers, provide a route to stretchable and conducting composites incorporating nanowires, nanoparticles,[7] and nanocarbons.[8,9] Nevertheless, their electrical conductance decreases with high tensile strain,[10,11] which results in the variable power and voltage requirements affecting the functions of, for instance, biosensors. Furthermore, the strain-induced structural changes in the nanoscale composites are complex involving fascinating multiscale structural reorganization and self-assembly processes.[12,13] They, however, remain difficult to predict, which makes the design of the conductive composites with desired conductance/strain property differential difficult.

Stretchable multiscale constructs have attracted increasing attention in recent years. For example, electronic materials patterned in fractal motifs[14,15] or noncoplanar arc-shaped structures[16] bonded to elastomers have been explored. These strategies require relatively expensive microfabrication techniques and complicated transfer processes. Wrinkled or waved conductive belts/membranes on elastomers have also been fabricated to achieve the combination of stretchability and conductivity.[17–19] However, delamination is known to occur under repeated stretching or compressing deformations for these structures.[20] Therefore, the problem of combining efficient charge transport and high strain is not yet practically solved and is further complicated by the strong dependence of conductivity on strain. It is desirable to develop a simple, scalable, and cost-effective method for fabricating highly stretchable conductors in which charge transports would be independent of the degree or direction of the deformation.

Inspired by kirigami, the art of paper cutting, the stretchability of materials can be tailored via cutting and shape deformations.[21,22] For instance, the stretchability of nanocarbon composites and graphene layers can be dramatically enhanced by introducing the kirigami patterns.[23–25] The tensile yield

and fracture strains of monolayer MoS_2 substantially increase with kirigami processing.[21] With respect to applications, stretchable kirigami conductors were demonstrated to serve as solar trackers,[26] tunable plasma electrodes,[25] and tunable kirigami diffraction gratings generated by photolithographic processes.[27] The kirigami process is theoretically and experimentally capable of changing the morphology of a material's structure from the micro-scale to bulk. The conductance of all the kirigami sheets previously reported never exceeded 0.02 S.[23,25]

Here, we report a highly conductive film with silver nanoparticles (Ag NPs) incorporated in a porous aramid nanofiber (ANF) matrix. ANFs are derived from well-known ultrastrong Kevlar macroscale fibers™ that impart high mechanical performance to ANF and to composites made on ANF basis.[28–30] These nanofibers also reveal unique branched morphology that allows them to easily assemble into nanoporous networks advantageous for efficient charge and stress transfer.[31] Furthermore, ANFs are highly biocompatible and can be used even for implantable devices.[32] The as-prepared Ag/ANF films have a conductivity of 1420 S cm^{-1}. The distinctive thermal resilience of the aramid chains in Kevlar™ enables annealing at temperatures as high as 200 °C, which the conductivity dramatically increases to 230 000 S cm^{-1}. By applying a simple kirigami pattern with parallel notches, the film becomes highly stretchable when loading the stress perpendicular to the cuts. The ultimate elongation increases from ∼2% to beyond 100%, and the conductance remains unchanged over the entire strain region.

The schematic illustration of the overall process for the fabrication of a Ag/ANF film with the kirigami pattern is shown in Fig. 1(a). The ANF solution was prepared as reported previously[28] and the ANF films were fabricated through a spin-coating process from a 2 wt. % ANF solution, where the nanofibers have a branched morphology.[31] The transparent, flexible ANF alcogel formed and detached from glass substrates after immersion in ethanol for 4 h. Switching solvents from previously used dimethyl sulfoxide (DMSO) to ethanol allowed for protonation of the amide groups on the ANFs and also enhanced the delamination of the films from glass substrates.[33,34] The Ag NPs were synthesised by reducing silver nitrate ($AgNO_3$) with sodium borohydride ($NaBH_4$) in the presence of poly(vinyl pyrrolidone) (PVP) as a stabilizer.[35] The Ag/ANF composites were fabricated by infiltrating Ag NPs into the free standing ANF films via vacuum-assisted filtration.[12,34] After drying, the Ag/ANF composite films were annealed at different temperatures. The kirigami patterns were made using a razor blade; the length of the cut, L, was 7.5 mm, and the spacings in the horizontal and vertical directions were $x = 2.5$ mm and $y = 1.5$ mm, respectively.

The scanning electron microscopy (SEM) images in Figs. 1(b), 1(c), and Fig. S1 (supplementary material) show the porous structures of the ANF films. This open structure provides enough space through which the Ag NPs can infiltrate into the films. The diameters of the spherical Ag NPs are in the range of 10–30 nm [Fig. S2(a) (supplementary material)]. This wide distribution in NP diameter enhances the conductivity of the Ag/ANF composite due to the smaller Ag NPs filling the spaces between the larger ones. The UV-Vis spectrum of the Ag NPs in solution [Fig. S2(b) (supplementary material)] shows a plasmon peak at 399 nm, which is typical for spherical silver NPs. The SEM images in Fig.
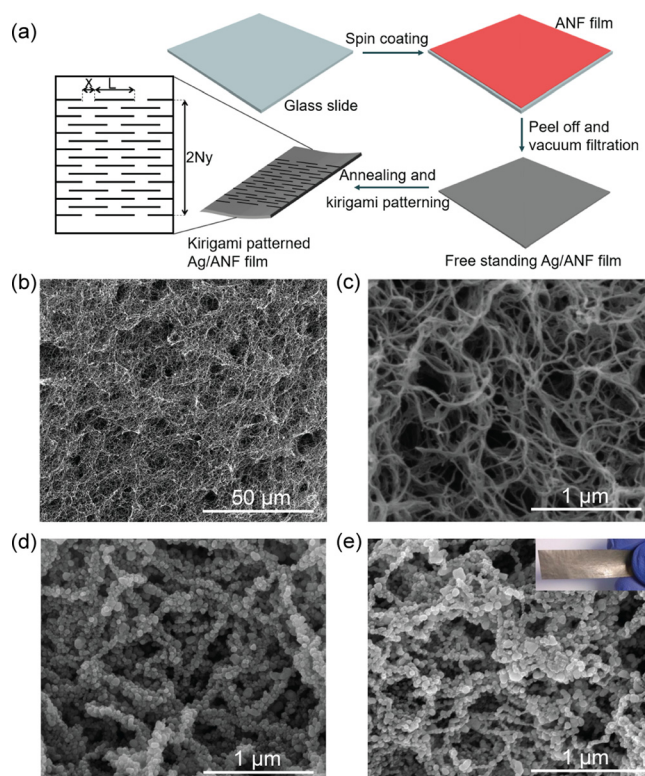

FIG. 1. (a) Schematic illustration of the process to prepare the Ag/ANF film with the kirigami pattern. SEM images of ANF films with (b) low and (c) high resolution. The SEM image of the (d) as-prepared and (e) annealed Ag/ANF films. The inset in (e) is a photograph of the Ag/ANF composite.

1(d) show the morphologies of the Ag/ANF films, where the Ag NPs uniformly envelope the ANFs, forming a three dimensional percolating network throughout the entire material. The forces between NPs and ANFs include a large component of hydrogen bonds as can be concluded from FT-IR spectroscopy [Fig. S3 (supplementary material)]. After a mild thermal annealing process, the Ag NPs in Ag/ANF films aggregated due to the coalescence of the active surface atoms of the NPs [Fig. 1(e)]. The inset in Fig. 1(e) is a photograph of the free-standing Ag/ANF film with a thickness of about 10 μm [Fig. S4 (supplementary material)].
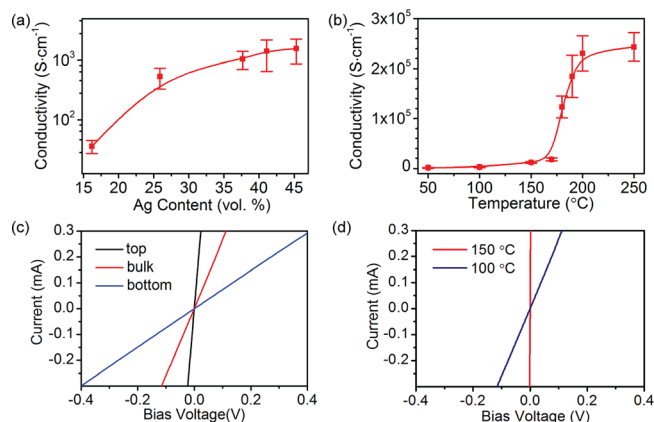

FIG. 2. Electrical conductivity of Ag/ANF composite films. Conductivity of Ag/ANF films as a function of (a) Ag NPs' volumetric fraction and (b) annealing temperature. (c) IV characteristic measured along the top and bottom surfaces of the 100 °C annealed film compared with that measured through the film thickness (bulk). (d) The through-film bulk IV characteristic for the 100 °C and 150 °C annealed films.
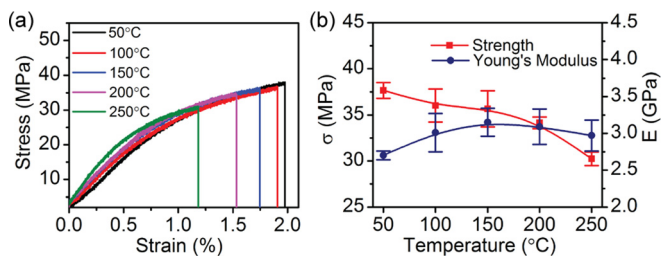
FIG. 3. Mechanical properties of Ag/ANF composites. (a) Stress-strain curves. (b) Dependences of strength and Young's modulus of Ag/ANF films as a function of annealing temperature.

FIG. 5. Conducting kirigami patterned nanocomposites with the zero conductance gradient. (a) Electrical conductance versus strain of 100 °C and 150 °C annealed Ag/ANF films. (b) Variation in the IV characteristic of the 100 °C annealed Ag/ANF film cut into a kirigami pattern as the top-surface is probed along the arms of the pattern (A–F) maintaining the base contact point at O, as shown in the inset.

Figure 2(a) shows the electrical conductivity of the Ag/ANF films as a function of Ag fraction from 16.2 vol. % to 45.3 vol. %. The Ag fraction calculations were based on the Ag mass content, which was measured by thermogravimetric analysis [TGA, Fig. S5 (supplementary material)]. At a Ag concentration of 16.2 vol. %, the conductivity was 36 S cm^{-1}; however, as the Ag content increased to 25.9 vol. % and 34.7 vol. %, a dramatic rise in the conductivity was observed, resulting in conductivities of 536 S cm^{-1} and 1060 S cm^{-1}, respectively, originating from formation of self-assembled percolation pathways in the material. Further increased Ag loading to 41.1 vol. % and 45.3 vol. % resulted in only slightly increased conductivities to 1420 S cm^{-1} and 1570 S cm^{-1}, respectively. Figure 2(b) presents the electrical conductivity of Ag/ANF films (41.1 vol. % Ag NPs) as a function of annealing temperature, while the annealing time was maintained at 4 h. When the temperature was below 150 °C, the increase in conductivity as a function of temperature was slow. Conductivity increased rapidly between 150 and 200 °C due to the partial coalescence of Ag nanoparticles resulting in lattice-to-lattice connectivity between them. The increased intensities of the X-ray diffraction (XRD) peaks provide evidence that thermal annealing improved the Ag NPs' crystallinity and reduced crystal defects [Fig. S6 (supplementary material)]. After thermal annealing at 200 °C, the conductivity of the films was observed to be as high as 230 000 S cm^{-1}, which is approaching the conductivity of many metals. A further increase in the annealing temperature to 250 °C elevated the conductivity to 243 000 S cm^{-1}. The conductivity of Ag/ANF films at different temperatures as a function of annealing time is provided in Fig. S7 (supplementary material). The mechanisms of conduction in the Ag/ANF films were also investigated. Figure S8 (supplementary material) shows the temperature dependence of the conductivity for 100 °C and 200 °C annealed Ag/ANF films, where the conductivity linearly declines with increasing temperature from 5 K to 300 K, indicating metallic conduction behavior.

The uniformity of the conductance throughout the depth of the film can be gauged by evaluating the current-voltage (IV) characteristic on both the surface and through the bulk. As shown in Fig. S9 (supplementary material), the conductance can vary slightly as the probe tip pressure, applied to the film surface, is modified because the flexibility of the Ag/ANF film can affect the area of the contact as well as the degree of film compression. Thus, in all subsequent experiments, a constant probe tip pressure (1.9 kPa) was applied. The current-voltage curves for the 100 °C annealed Ag/ANF film [Fig. 2(c)] show that even the films with moderate annealing exhibited conductivity suitable for the majority of the devices. Although the top-most surface has the highest conductivity, the resistivity is low throughout the bulk and at the bottom surface. The substantial increase in conductivity as the annealing temperature increases from 100 °C to 150 °C is reflected in the through-film bulk IV curves [Fig. 2(d)].

Figure 3(a) shows the stress-strain behavior of the Ag/ANF films annealed at different temperatures. The tensile strain decreased from 2.0% to 1.2% and the strength declined from 37.7 MPa to 30.2 MPa as the temperature was increased from 50 °C to 250 °C. However, the Young's modulus increased from 2.7 GPa to 3.1 GPa when the annealing temperature increased from 50 °C to 150 °C, which is attributed to the sintering of the Ag NPs at higher temperature. Further increases in the annealing temperature resulted in a slight decrease of the Young's modulus [Fig. 3(b)]. There is a trade-off relationship between improved conductivity and degraded mechanical properties with regard to the annealing temperatures. Therefore, the optimal annealing temperature was chosen to be 200 °C, which gives composites with an electrical conductivity of 230 000 S cm^{-1}, a tensile strength of 34.1 MPa, and a Young's modulus of 3.1 GPa.
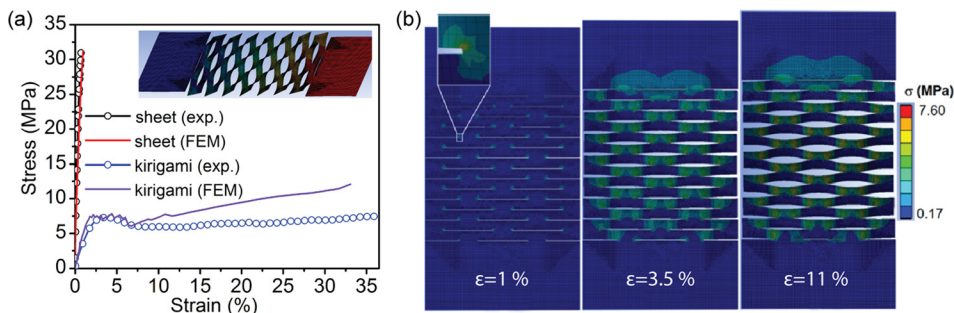

FIG. 4. FEM results. (a) Stress-strain curves for non-patterned and kirigami-patterned sheets, both experimentally measured (dotted lines) and FEM results (solid lines). The inset shows the deformed shape of the kirigami-film at 21% strain. (b) Spatial evolution of the maximum principal stress in the kirigami patterned Ag/ANF film as the solid is deformed, for one strain below buckling (1%) and two strains following bi-stable deformation (3.5% and 11%).
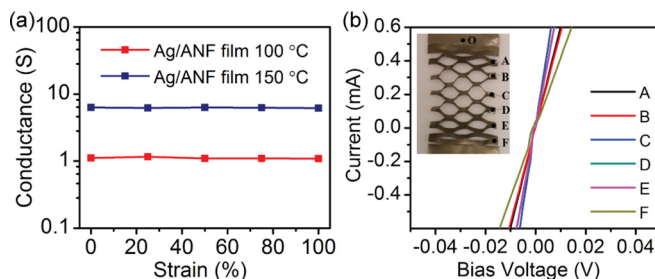
TABLE I. Electrical conductivity and conductance gradient of typical stretchable conducting materials.

Materials	Conductivity (S cm^{-1})	Conductance gradient (S/percent)	Stretchable strategies	References
Composite mat of poly(styrene-block-butadiene-block-styrene) (SBS) fibres and Ag NPs	~5400	−0.48	Elastomer fibres mat	37
Buckled Cu layer adhered on PDMS	160 000	−0.009	Elastomer with prestrain	38
Hybrid Ag–multiwalled carbon nanotubes (MWNT) composite film	5710	−0.54	Composite from blending	39
EGaIn filled in 3D porous PDMS	~24 100	~0	Net-shaped 3D structure	40
Composites from ANF and Ag NPs	230 000	~0	Kirigami structure	This work

Finite element modelling (FEM) was used to investigate the stress-strain response of pristine and kirigami patterned Ag/ANF films. The experimental stress-strain results of the corresponding films are also presented for comparison [Fig. 4(a)]. For pristine films, the deformation occurs via the in-plane stretching of Ag/ANFs within the matrix; the stress grows unabated until structural failure (black dotted line). The FEM stress-strain curve of the pristine film (solid red line) shows tensile behavior similar to its experimental result. For the kirigami film, the initial elasticity growth resembles the deformation curve of the pristine films, indicating that the deformation is initially restricted to the in-plane stretching. When the applied tensile stress exceeds a critical buckling load (corresponding to 7.5 MPa in the figure), the planar deformation is unstable, and the strips start to bend and twist out-of-plane [Fig. 4(a) inset]. The kirigami films exhibit out-of-plane deflection due to a mechanical bi-stability detailed in previous reports.[25,36] The subsequent motion of the rotating strips distributes the stress growth into the bending and torsional modes, an out-of-plane deformation that enables the kirigami-film to enhance the stretchability of the solid. The FEM (solid purple line) replicates the general stress-strain trends observed in the experiments (blue dotted line), revealing that the geometric parameters and boundary conditions are in agreement with our understandings. The FEM-derived maximum principal stress distribution in the kirigami patterned Ag/ANF film as it is deformed is presented in Fig. 4(b). It demonstrates that although the stress is initially concentrated at the interior corners of the cuts, the kirigami pattern can divert the stress growth into bending modes and thereby effectively control the deformation. Subsequent deformation is localized at the edge of the cuts, leading to hardening of the materials and finally to fracture.

Compared with pristine Ag/ANF films, the tensile strain of Ag/ANF kirigami-films increased to more than 100%, and the films can be reversibly stretched. Figure S10 (supplementary material) shows images of the kirigami patterned Ag/ANF films at different strains (0, 25%, 50%, 75%, and 100%). It is worth noting that the extension of the kirigami films can be further improved by increasing the cut length and decreasing the spacing between the cuts. Generally, increasing the cut length softens the material, and increased spacing between the cuts makes the sheet more rigid.[26]

Importantly, the kirigami-structured films are not only highly stretchable but also retain remarkable conductance. As shown in Fig. 5(a), the conductance of Ag/ANF films that annealed at 100 °C and 150 °C remained nearly constant during stretching. Figure 5(b) shows the surface (top) current measured between an arm of the pattern (A–F) and the fixed contact point (O) on the edge of the Ag/ANF film [Fig. 5(c) inset]. The relative constancy of the IV curves as one takes measurements across the pattern demonstrates that the increase in resistance that accompanies a longer conductive path is small compared with the measurement variability associated with replacing the contact upon the film. The excellent conductance is maintained along the entire kirigami pattern. The resistance derived from the slopes and across the six measured (and averaged) positions is 16.3 ± 5.9 Ω.

The electrical conductivity and conductance gradient of kirigami-structured Ag/ANF films are compared with those of other typical stretchable conducting materials in Table I. The comparison indicates that kirigami patterned Ag/ANF films with higher conductivity and zero conductance gradient occupy a special place among stretchable conductors. The macroscale composite made from the polydimethylsiloxane channel network filled with liquid metal—the eutectic Ga-In alloy (EGaIn)—may also display the zero conductance gradient. However, this ability is limited by the melting point of Ga-based liquid metals which is reported to be between −19 °C and +11 °C. Liquid mercury can expand this range to −38.8 °C. Considering the widely discussed applications of stretchable conductors as skin-contact sensors and electronics, toxicity can be problematic for both types of composites based on liquid metals.

In conclusion, stretchable composite conductors with high electrical conductivity and high stretchability were obtained by the incorporation of Ag NPs into the percolating network of branched ANFs. The optimized films showed a conductivity of 230 000 S cm^{-1}, an ultimate strength of 34.1 MPa, and a Young's modulus of 3.1 GPa. After kirigami patterning, the tensile strain of Ag/ANF composite films increased from 1% to 2% to >100%, while the conductance remained constant during stretching. Combined with solid state nature of the material and its biocompatibility, this property is expected to be essential for flexible and wearable electronic devices, among other applications.

See supplementary material for the Ag/ANF film preparations, finite-element modelling, and characterization.

[1]A. Sekiguchi, F. Tanaka, T. Saito, Y. Kuwahara, S. Sakurai, D. N. Futaba, T. Yamada, and K. Hata, Nano Lett. **15**, 5716 (2015).

[2]D. Son, J. H. Koo, J.-K. Song, J. Kim, M. Lee, H. J. Shim, M. Park, M. Lee, J. H. Kim, and D.-H. Kim, ACS Nano **9**, 5585 (2015).

[3]M. Lee, K. Lee, S. Kim, H. Lee, J. Park, K. Choi, H. Kim, D. Kim, D. Lee, S. Nam, and J. Park, Nano Lett. **13**, 2814 (2013).

[4]Y.-L. Park, B.-R. Chen, and R. J. Wood, IEEE Sens. J. **12**, 2711 (2012).

[5]J. Lessing, S. A. Morin, C. Keplinger, A. S. Tayi, and G. M. Whitesides, Adv. Funct. Mater. **25**, 1418 (2015).

[6]J. A. Rogers, T. Someya, and Y. Huang, Science **327**, 1603 (2010).

[7]J. Ge, H.-B. Yao, X. Wang, Y.-D. Ye, J.-L. Wang, Z.-Y. Wu, J.-W. Liu, F.-J. Fan, H.-L. Gao, C.-L. Zhang, and S.-H. Yu, Angew. Chem. **125**, 1698 (2013).

[8]D. J. Lipomi, M. Vosgueritchian, B. C.-K. Tee, S. L. Hellstrom, J. A. Lee, C. H. Fox, and Z. Bao, Nat. Nanotechnol. **6**, 788 (2011).

[9]K. S. Kim, Y. Zhao, H. Jang, S. Y. Lee, J. M. Kim, K. S. Kim, J.-H. Ahn, P. Kim, J.-Y. Choi, and B. H. Hong, Nature **457**, 706 (2009).

[10]Z. Chen, W. Ren, L. Gao, B. Liu, S. Pei, and H.-M. Cheng, Nat. Mater. **10**, 424 (2011).

[11]L. Hu, W. Yuan, P. Brochu, G. Gruner, and Q. Pei, Appl. Phys. Lett. **94**, 161108 (2009).

[12]Y. Kim, J. Zhu, B. Yeom, M. Di Prima, X. Su, J.-G. Kim, S. J. Yoo, C. Uher, and N. A. Kotov, Nature **500**, 59 (2013).

[13]J. Xu, S. Wang, G. N. Wang, C. Zhu, S. Luo, L. Jin, X. Gu, S. Chen, V. R. Feig, J. W. F. To, S. Rondeau-Gagné, J. Park, B. C. Schroeder, C. Lu, J. Y. Oh, Y. Wang, Y. Kim, H. Yan, R. Sinclair, D. Zhou, G. Xue, B. Murmann, C. Linder, W. Cai, J. B.-H. Tok, J. W. Chung, and Z. Bao, Science **355**, 59 (2017).

[14]J. A. Fan, W.-H. Yeo, Y. Su, Y. Hattori, W. Lee, S. Jung, Y. Zhang, Z. Liu, H. Cheng, L. Falgout, M. Bajema, T. Coleman, D. Gregoire, R. J. Larsen, Y. Huang, and J. A. Rogers, Nat. Commun. **5**, 3266 (2014).

[15]L. Xu, S. R. Gutbrod, Y. Ma, A. Petrossians, Y. Liu, R. C. Webb, J. A. Fan, Z. Yang, R. Xu, J. J. Whalen, J. D. Weiland, Y. Huang, I. R. Efimov, and J. A. Rogers, Adv. Mater. **27**, 1731 (2015).

[16]D.-H. Kim, J. Song, W. M. Choi, H.-S. Kim, R.-H. Kim, Z. Liu, Y. Y. Huang, K.-C. Hwang, Y. Zhang, and J. A. Rogers, Proc. Natl. Acad. Sci. U.S.A. **105**, 18675 (2008).

[17]D. Qi, Z. Liu, M. Yu, Y. Liu, Y. Tang, J. Lv, Y. Li, J. Wei, B. Liedberg, Z. Yu, and X. Chen, Adv. Funct. Mater. **27**, 3145 (2015).

[18]Y. Zhu and F. Xu, Adv. Mater. **24**, 1073 (2012).

[19]S. P. Lacour, S. Wagner, Z. Huang, and Z. Suo, Appl. Phys. Lett. **82**, 2404 (2003).

[20]F. Xu and Y. Zhu, Adv. Mater. **24**, 5117 (2012).

[21]P. Z. Hanakata, Z. Qi, D. K. Campbell, and H. S. Park, Nanoscale **8**, 458 (2016).

[22]L. Xu, T. C. Shyu, and N. A. Kotov, ACS Nano **11**, 7587 (2017).

[23]M. K. Blees, A. W. Barnard, P. A. Rose, S. P. Roberts, K. L. McGill, P. Y. Huang, A. R. Ruyack, J. W. Kevek, B. Kobrin, D. A. Muller, and P. L. McEuen, Nature **524**, 204 (2015).

[24]Z. Qi, H. S. Park, and D. K. Campbell, preprint arXiv:1407.8113 (2014).

[25]T. C. Shyu, P. F. Damasceno, P. M. Dodd, A. Lamoureux, L. Xu, M. Shlian, M. Shtein, S. C. Glotzer, and N. A. Kotov, Nat. Mater. **14**, 785 (2015).

[26]A. Lamoureux, K. Lee, M. Shlian, S. R. Forrest, and M. Shtein, Nat. Commun. **6**, 8092 (2015).

[27]L. Xu, T. C. Wang, Y. Kim, T. C. Shyu, J. Lyu, and N. A. Kotov, ACS Nano **10**, 6156 (2016).

[28]M. Yang, K. Cao, L. Sui, Y. Qi, J. Zhu, A. Waas, E. M. Arruda, J. Kieffer, M. D. Thouless, and N. A. Kotov, ACS Nano **5**, 6945 (2011).

[29]J. Zhu, W. Cao, M. Yue, Y. Hou, J. Han, and M. Yang, ACS Nano **9**, 2489 (2015).

[30]S.-O. Tung, S. Ho, M. Yang, R. Zhang, and N. A. Kotov, Nat. Commun. **6**, 6152 (2015).

[31]J. Zhu, M. Yang, A. Emre, J. H. Bahng, L. Xu, J. Yeom, B. Yeom, Y. Kim, K. Johnson, P. Green, and N. A. Kotov, Angew. Chem., Int. Ed. **129**, 11906 (2017).

[32]L. Xu, X. Zhao, C. Xu, and N. A. Kotov, "Water-rich biomimetic composites with abiotic self-organizing nanofiber network," Adv. Mater. (to be published).

[33]K. Cao, C. P. Siepermann, M. Yang, A. M. Waas, N. A. Kotov, M. D. Thouless, and E. M. Arruda, Adv. Funct. Mater. **23**, 2072 (2013).

[34]J. Lyu, X. Wang, L. Liu, Y. Kim, E. K. Tanyi, H. Chi, W. Feng, L. Xu, T. Li, M. A. Noginov, C. Uher, M. D. Hammig, and N. A. Kotov, Adv. Funct. Mater. **26**, 8435 (2016).

[35]L. Polavarapu, K. K. Manga, H. D. Cao, K. P. Loh, and Q. H. Xu, Chem. Mater. **23**, 3273 (2011).

[36]M. Isobe and K. Okumura, Sci. Rep. **6**, 24758 (2016).

[37]M. Park, J. Im, M. Shin, Y. Min, J. J. Park, H. Cho, S. Park, M.-B. Shim, S. Jeon, D.-Y. Chung, J. Bae, J. J. Park, U. Jeong, and K. Kim, Nat. Nanotechnol. **7**, 803 (2012).

[38]X. Wang, H. Hu, Y. Shen, X. Zhou, and Z. Zheng, Adv. Mater. **23**, 3090 (2011).

[39]K.-Y. Chun, Y. Oh, J. Rho, J.-H. Ahn, Y.-J. Kim, H. R. Choi, and S. Baik, Nat. Nanotechnol. **5**, 853 (2010).

[40]J. Park, S. Wang, M. Li, C. Ahn, J. K. Hyun, D. S. Kim, D. K. Kim, J. A. Rogers, Y. Huang, and S. Jeon, Nat. Commun. **3**, 916 (2012).